

Enhancing the Secrecy Rate with Direction-range Focusing with FDA and RIS

Chu Li, Stefan Roth and Aydin Sezgin

Ruhr-Universität Bochum, Germany

Email: {chu.li, stefan.roth-k21, aydin.sezgin}@rub.de

Abstract—One of the great potentials to improve the confidentiality in mmWave/THz at the physical layer of technical communication, measured by the secrecy rate, lies in the use of reconfigurable intelligent surfaces (RISs). However, an important open problem arises when the eavesdropper is aligned with the legitimate user or in proximity to the RIS or legitimate user. The limitation comes, on one hand, from the high directional gain caused by the dominant line-of-sight (LOS) path in high-frequency transmission, and, on the other hand, from the high energy leakage in the proximity of the RIS and the legitimate user. To address these issues, we employ the concept of frequency diverse arrays (FDA) at the base station (BS) associated with random inverted transmit beamforming and reflective element subset selection (RIBES). More specifically, we consider a passive eavesdropper with unknown location and design the transmit beamforming and RIS configuration based on the channel information of the legitimate user only. In this context, the secrecy rate with the proposed transmission technique is evaluated in the case of deterministic eavesdropper channel, demonstrating that we can ensure a secure transmission regarding both direction and range. Furthermore, assuming no prior information about the eavesdropper, we describe the wiretap region and derive the *worst-case secrecy rate* in closed form. The latter is further optimized by determining the optimal subset sizes of the transmit antennas and reflective elements. Simulations verify the correctness of the closed-form expressions and demonstrate that we can effectively improve the secrecy rate, especially when the eavesdropper is close to the RIS or the legitimate user.

Index Terms—Reconfigurable intelligent surfaces, physical layer security, secrecy rate, frequency diverse array, inverted beamforming, reflective elements selection

I. INTRODUCTION

Security has always been a major concern in wireless communication systems, and it becomes even more crucial in 6G networks. In most current communication standards, security aspects are implemented on higher layers, where cryptography-based methods can be applied. However, the implementation of these technologies in 6G networks faces significant challenges due to the proliferation of low-resource devices and the existence of heterogeneous networks [1]. To complement cryptography-based methods and effectively meet the security requirements in future networks, physical layer security is envisioned as a promising solution [2]–[4]. Furthermore, to enhance the performance of the physical layer security technique, reconfigurable intelligent surfaces (RISs) have emerged as a promising solution. RIS is a plain

surface consisting of massive, low-cost reflective elements with configurable amplitude and phase. Due to its configurable properties, RISs exhibit significant potentials in improving communication quality [5]–[7], enhancing network resilience [8], advancing localization and sensing capabilities [9]–[11], and contributing to various aspects of covert communication [12] and physical layer security [13]–[20].

The secrecy rate performance in RIS-assisted systems has been investigated in numerous recent works. In [15]–[17], the secrecy rate is optimized by a joint design of the transmit beamforming and RIS phase shifts. The works [18]–[20] additionally utilize artificial noise to improve the secrecy rate in an RIS-assisted system. However, the approaches proposed in the aforementioned works to optimize the secrecy rate assume the channel state information of the legitimate user and the eavesdropper are uncorrelated and independent. Under such assumption, the transmit beamforming and RIS are jointly designed to enhance the received signal at the legitimate receiver while simultaneously weaken the received signal at the eavesdropper, thus improving secrecy. However, these approaches become ineffective in mmWave/THz communication systems, if the eavesdropper is spatially aligned with the legitimate user or in proximity to the legitimate user or RIS. In this case, the channels of the legitimate user and the eavesdropper are highly correlated, primarily due to the dominant line-of-sight (LOS) path. Moreover, compared to transmission in low and moderate frequencies, the channel gain in mmWave/THz attenuates more rapidly with an increasing propagation path. Note that an eavesdropper located close to the RIS may experience a significantly larger channel gain compared to that of the legitimate user. Hence, an eavesdropper at this location may have the ability to decode the transmitted signal correctly.

To decorrelate the channels of receivers in close proximity to each other, frequency diverse array (FDA) has been proven as a promising technique in many recent studies [21]–[24]. FDA was initially proposed in [25], subsequently gaining significant attention in radar applications [26]–[29]. By exploiting a minor frequency shift across the antennas, FDA can generate a direction-range-dependent beam pattern. Thus, it can be also used for improving the physical layer security performance in terms of secrecy rate and covert rate in mmWave/THz transmission [22]–[24], [30]–[32]. More specifically, by solving different non-convex optimization problems, the frequency shift at each antenna is carefully designed to optimize the secrecy rate in [22], [23] and the covert rate in [24]. In these works, the optimization problem is solved by assuming either

This work was supported by the German Federal Ministry of Education and Research (BMBF) project 6G-ANNA [grant agreement number 16KISK095].

full or partial information about the eavesdropper, which is challenging to obtain in practice. Alternatively, random FDA is utilized to enhance the secrecy rate in [30], [31] and covert rate in [32]. However, such approach may lead to an increase in the circuit cost at the transmitters. Moreover, direct transmission is prone to blockages in mmWave/THz. To address this issue, an RIS can be employed to establish an additional strong communication path between transceivers [33]. Different to the above works, we investigate the secrecy performance in an RIS-assisted system with FDA in the presence of a passive eavesdropper.

Furthermore, the eavesdropper can position itself in any of various vantage locations to intercept confidential messages. Therefore, it is crucial to develop an approach that safeguards the transmission in all circumstances. To resist against an eavesdropper in any undesired directions, the works [34], [35] utilize a random transmit antenna switching technique. In this approach, the transmitted signal is intentionally degraded in any undesired direction, such that the overall secrecy performance is enhanced. More specifically, a random antenna subset is selected for each transmit symbol to perform beamforming, while the remaining antennas are turned off. Additionally, a new random selection is generated for each following transmit symbol. However, such kind of sparse antenna array configuration provides an opportunity for a smart eavesdropper capable of conducting measurements at different locations to intercept and recover the transmitted signal [36]. In addition, the use of switched antenna technique requires a switch at each antenna that controls the ON-OFF status. Subsequently, random inverted transmit antennas are utilized in [37]–[40], also referred to as randomized radiation or randomized beamforming. In this technique, a random subset of the transmit antennas is selected for conventional beamforming, while the inverted beamforming, i.e., conventional beamforming with an additional weight of $e^{j\pi} = -1$, is performed at the remaining antennas. As all antennas are active during the transmission, switching between states is not needed. Furthermore, the work [13] proposed reflective element subset selection (ESS) in RIS-assisted secure systems, where a subset of the reflective elements is selected to enhance the secrecy rate.

Contribution: In this work, we develop a transmission technique for RIS-assisted systems that ensures secure communication regarding direction and range, without requiring prior information about the eavesdropper. To this end, we propose random inverted transmit beamforming and reflective element subset selection (RIBES), to be utilized jointly with a FDA at the BS. More specifically, we investigate the secrecy rate performance in mmWave/THz systems, where a BS communicates with a legitimate receiver Bob, in the presence of a passive eavesdropper Eve. We demonstrate that security in terms of confidentiality can be achieved through the proposed transmission technique. This holds even with a simple linear FDA, where the frequency shift between neighboring antennas remains the same. The main contributions are as follows:

- We employ FDA at the BS with RIBES, considering the presence of a passive eavesdropper. In this context, we design the transmit beamforming and RIS configuration to maximize the received SNR at Bob.

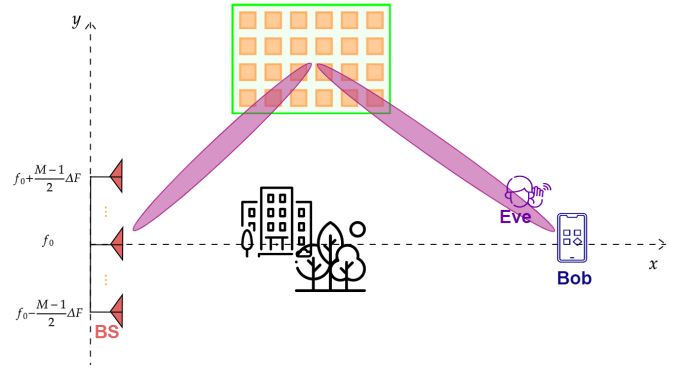


Fig. 1: RIS-assisted secure transmission with FDA at the BS in the presence of an eavesdropper

- Applying the proposed transmit beamforming and RIS configuration, we define the scaling factor of the received signal and derive its statistical properties, laying the foundation for analyzing secrecy performance. Afterwards, we analyze and derive closed-form expressions for the secrecy rate, both with and without employing FDA and RIBES.
- We formulate a definition of the wiretap area for the proposed transmission technique. Furthermore, assuming Eve is located within the wiretap area, we derive the upper bound of the received SNR at Eve.
- Based on the above derivations, we find a closed-form expression for the optimal subset sizes of the transmit antennas and reflective elements that maximize the *worst-case secrecy rate*. In addition, we simplify the expressions for the case where the received SNR at Bob is significantly larger than 0 dB.
- We determine the optimal frequency increment that maximizes the secrecy performance given the channel information of Eve. The resulting secrecy rate is considered as an upper bound in this work.

Organization: The rest of the paper is organized as follows. We introduce the system model in Sec. II. Afterwards, the proposed transmit beamforming and RIS configuration with RIBES are provided in Sec. III. Subsequently, we analyze the secrecy rate with and without the use of FDA and RIBES in Sec. IV. Then, the proposed RIBES algorithm is optimized in Sec. V. We present the theoretical results corroborated with the simulation results in Sec. VI. Finally, Sec. VII concludes the paper.

Notation: Throughout this paper, boldface lower and upper case symbols are used to denote the vectors and matrices, respectively. $(\cdot)^H$ and \circ represent the Hermitian transpose operator and Hadamard product. The notation $\mathbf{X}_{i,j}$ indicates the element at position (i, j) of the \mathbf{X} . $[x]^+$ is a short form for $\max(0, x)$. The integer closest to x is denoted as $\lfloor x \rfloor$. The expectation and variance operator are denoted as $\mathbb{E}[\cdot]$ and $\mathbb{V}[\cdot]$, respectively.

II. SYSTEM MODEL

We consider RIS-assisted secure (confidential) transmission in a mmWave/THz system as shown in Fig. 1, where a M -antenna BS is communicating with a single-antenna legitimate

receiver, Bob, in the presence of a passive eavesdropper equipped with a single antenna, Eve. Furthermore, we consider a two-dimensional area, where the BS has equally spaced antennas and is positioned at the origin. We assume that direct transmission from the BS to all users is obstructed by blockage. To overcome this blockage, we employ an RIS positioned at $[x_{\text{RIS}}, y_{\text{RIS}}]$ to establish LOS links between the BS and the RIS, as well as between the RIS and the receivers. In addition, the RIS consists of a total of $N = N_V \times N_H$ reflecting elements, where N_V and N_H represent the number of elements per column and row, respectively. In addition, we assume all components of the RIS-assisted system are situated in the far field.

In this work, we utilize FDA at the BS to establish a secure transmission with both direction and range protection. In this particular configuration, the radiation frequency at the m -th antenna is written as

$$\begin{aligned} f_m &= f_0 + \Delta f_m \\ &= f_0 + \left(m - \frac{M+1}{2}\right) \Delta F, \quad m \in \{1, \dots, M\}, \end{aligned} \quad (1)$$

where f_0 is the center frequency, Δf_m represents the frequency shift at m -th transmit antenna, and ΔF denotes the frequency increment between adjacent antennas. Furthermore, in this study, we assume that the frequency shift Δf_m is significantly smaller than the center frequency. More specifically, we impose a constraint on the maximal frequency shift, i.e., $\max_m(\Delta f_m) < 10^{-3} f_0$.

It is noted that we are considering mmWave/THz transmission, where the LOS component dominates over the NLOS components due to high spreading, reflection, and scattering losses [22]. Therefore, in this work, we exclusively focus on the dominant LOS component and model the mmWave/THz channel according to the geometry channel model with one dominant component [7], [38], [41]. More specifically, we use $\mathbf{G} \in \mathbb{C}^{M \times N}$ to represent the BS-RIS channel, where the element of \mathbf{G} at position (m, n) is given by

$$\mathbf{G}_{m,n} = \sqrt{L_G(R_1)} e^{-j2\pi f_m \tau_{m,n}^{\text{BS-RIS}}}, \quad (2)$$

in which $L_G(R_1)$ is the path loss with R_1 being the distance between the BS and RIS. Further, $\tau_{m,n}^{\text{BS-RIS}}$ in (2) is the propagation delay from the m -th transmit antenna to the n -th RIS element, and it is computed as

$$\begin{aligned} \tau_{m,n}^{\text{BS-RIS}} &= \frac{1}{c} \left(R_1 - \left(m - \frac{M+1}{2}\right) d_{\text{BS}} \sin(\theta_{\text{tx}}) \right. \\ &\quad \left. + \left(n_V - \frac{N_V+1}{2}\right) d_V \sin(\theta_{\text{tx}}) \right. \\ &\quad \left. + \left(n_H - \frac{N_H+1}{2}\right) d_H \cos(\theta_{\text{tx}}) \right). \end{aligned} \quad (3)$$

Here, $n_H = \text{mod}(n, N_H)$ and $n_V = \lfloor n/N_H \rfloor$ are the horizontal and vertical indices of the n -th element, where $n \in \{1, \dots, N\}$, respectively. In addition, d_{BS} represents the antenna separation at the BS, while d_H and d_V denote the horizontal width and vertical height of each reflective element, respectively. Furthermore, we consider the setup $d_{\text{BS}} = d_H = d_V = \frac{c}{2f_0}$, where c denotes the speed of light.

Moreover, we have $\theta_{\text{tx}} = \arcsin\left(\frac{y_{\text{RIS}}}{R_1}\right)$ representing the angle of departure (AOD) at the BS. Note that, within the considered two-dimensional geometric scenario, the AOD at the BS is equal to the angle of arrival (AOA) at the RIS. Furthermore, since multiple frequencies are utilized at the BS, we represent the channel between RIS and the receiver using an $M \times N$ matrix, i.e., \mathbf{H}_{UE} , where the m -th column corresponds to the channel at frequency f_m . It is noted that $\text{UE} \in \{\text{B}, \text{E}\}$ can represent either Bob (the legitimate receiver) or Eve (the eavesdropper). Similar to (2), we have

$$\mathbf{H}_{\text{UE},(m,n)} = \sqrt{L_H(R_{\text{UE}})} e^{-j2\pi f_m \tau_n^{\text{RIS-UE}}}, \quad (4)$$

where $L_H(R_{\text{UE}})$ is the path loss of RIS-UE channel, and R_{UE} represents the distance between the RIS and the respective receiver. The propagation delay from the n -th reflective element to the receiver $\tau_n^{\text{RIS-UE}}$ can be computed as

$$\begin{aligned} \tau_n^{\text{RIS-UE}} &= \frac{1}{c} \left(R_{\text{UE}} + \left(n_V - \frac{N_V+1}{2}\right) d_V \sin(\theta_{\text{UE}}) \right. \\ &\quad \left. - \left(n_H - \frac{N_H+1}{2}\right) d_H \cos(\theta_{\text{UE}}) \right), \end{aligned} \quad (5)$$

in which θ_{UE} is the AOA at the receiver. Given that the receiver's location is specified as $[x_{\text{UE}}, y_{\text{UE}}]$, θ_{UE} can be computed by $\arccos\left(\frac{x_{\text{UE}} - x_{\text{RIS}}}{R_{\text{UE}}}\right)$.

In addition, we use $x(k) \in \mathbb{C}$ to represent the transmitted data symbol with unit variance, where k denotes the symbol index. Also, the transmit beamforming vector at the BS is represented by $\mathbf{w}(k) \in \mathbb{C}^{M \times 1}$. Thereby, the received signal can be expressed as

$$y_{\text{UE}}(k) = \sqrt{P} \mathbf{h}_{\text{UE}}^H \mathbf{w}(k) x(k) + n_{\text{UE}}(k), \quad (6)$$

where P is the transmit power, $n_{\text{UE}}(k)$ is the thermal noise at the receiver, distributed as $n_{\text{UE}} \sim \mathcal{CN}(0, \sigma_{\text{UE}}^2)$, and $\mathbf{h}_{\text{UE}} \in \mathbb{C}^{M \times 1}$ is the cascaded channel given by

$$\mathbf{h}_{\text{UE}} = (\mathbf{G} \circ \mathbf{H}_{\text{UE}}) \mathbf{v}. \quad (7)$$

Here, \mathbf{v} is the RIS vector, which can be expressed as

$$\mathbf{v} = [e^{j\phi_1}, \dots, e^{j\phi_n}, \dots, e^{j\phi_N}]^T, \quad (8)$$

where ϕ_n represents the phase shift of the n -th reflective element. The phase shifts can be dynamically adjusted by the BS. Thereby, we focus on a frequency-flat RIS configuration, i.e., the applied phase shifts are the same across all frequencies. This kind of configuration is utilized in the majority of studies that have explored multiple frequencies in RIS-assisted transmission [42]–[44]. Note that, frequency-selective phase shifts within an RIS can be realized by carefully designing the circuit topology of each reflective element [45]. However, such a design increases the hardware complexity.

III. TRANSMIT BEAMFORMING AND RIS DESIGN

We utilize the secrecy rate to evaluate the performance of the proposed method. Let γ_{B} and γ_{E} represent the received SNR at Bob and Eve, respectively. The secrecy rate, as defined in [46], can be expressed as

$$C_s(\gamma_{\text{B}}, \gamma_{\text{E}}) = [\log_2(1 + \gamma_{\text{B}}) - \log_2(1 + \gamma_{\text{E}})]^+. \quad (9)$$

Under the assumption of a passive eavesdropper, we design the transmit beamforming vector and RIS solely utilizing the value of the BS-to-Bob channel. In this work, we assume that perfect information of the BS-to-Bob channel is given at the BS. As a result, the optimal beamformer and RIS configuration that maximize the secrecy rate are equivalent to those that maximize the received SNR at Bob. In the following, we first introduce the conventional technique for optimizing transmit beamforming and RIS, and then we introduce the transmit beamforming and RIS design with RIBES.

A. Conventional transmit beamforming and RIS design

Maximizing the received SNR in a multiple-input single-output (MISO) system is a well-established problem [47]. In this context, the optimal strategy for transmit beamforming is maximum ratio transmission (MRT), which is

$$\mathbf{w} = \frac{\mathbf{h}_B}{\|\mathbf{h}_B\|}, \quad (10)$$

where, according to (7), $\mathbf{h}_B = (\mathbf{G} \circ \mathbf{H}_B)\mathbf{v}$. From this, the received SNR at Bob can be expressed as

$$\gamma_B = \frac{P}{\sigma_B^2} |\mathbf{h}_B^H \mathbf{w}|^2 = \frac{P}{\sigma_B^2} \text{tr}(\Psi \mathbf{V}), \quad (11)$$

where $\mathbf{V} = \mathbf{v}\mathbf{v}^H$ is a rank-one matrix, and $\Psi = (\mathbf{G} \circ \mathbf{H}_B)^H (\mathbf{G} \circ \mathbf{H}_B)$. The semidefinite relaxation (SDR) technique can be applied to find the optimal RIS configuration that maximizes γ_B [48]. By employing the above, the corresponding problem is formulated as

$$\begin{aligned} \max_{\mathbf{V}} \quad & \text{tr}(\Psi \mathbf{V}), \\ \text{s.t.} \quad & \mathbf{V}(n, n) = 1, \quad n = 1, \dots, N, \\ & \mathbf{V} \succeq 0. \end{aligned} \quad (12)$$

It's worth noting that the rank-one constraint of \mathbf{V} has been removed in order to obtain a convex problem. However, solving (12) does provide a useful upper bound for γ_B . In this work, we use this upper bound to evaluate the performance of the closed-form solution proposed in the following.

We now derive the closed-form solution for \mathbf{v} that maximizes the received SNR at Bob. Therefore, we first rewrite \mathbf{h}_{UE} in (7) with two auxiliary parameters $\tilde{\tau}_m$ and $\tilde{\tau}_n^{UE}$. By substituting (2), (3), (4) and (5) into (7), the m -th element of \mathbf{h}_{UE} is expressed as

$$\begin{aligned} \mathbf{h}_{UE,m} &= \sqrt{L_G(R_1)L_H(R_{UE})} \sum_{n=1}^N e^{-j2\pi f_m (\tau_{m,n}^{\text{BS-RIS}} + \tau_n^{\text{RIS-UE}})} e^{j\phi_n} \\ &= \sqrt{L_G(R_1)L_H(R_{UE})} e^{-j2\pi f_m \left(\frac{R_1 + R_{UE}}{c} + \tilde{\tau}_m \right)} \\ &\quad \times \sum_{n=1}^N e^{-j2\pi f_m \tilde{\tau}_n^{UE}} e^{j\phi_n}, \end{aligned} \quad (13)$$

where

$$\begin{aligned} \tilde{\tau}_m &= \frac{1}{c} \left(m - \frac{M+1}{2} \right) d_{\text{BS}} \sin(\theta_{\text{tx}}), \\ \tilde{\tau}_n^{UE} &= \frac{1}{c} \left(\left(n_V - \frac{N_V+1}{2} \right) d_V (\sin(\theta_{\text{tx}}) + \sin(\theta_{\text{UE}})) \right. \\ &\quad \left. + \left(n_H - \frac{N_H+1}{2} \right) d_H (\cos(\theta_{\text{tx}}) - \cos(\theta_{\text{UE}})) \right). \end{aligned} \quad (15)$$

Thus, the received SNR at Bob with MRT transmit beamforming can be computed as

$$\begin{aligned} \gamma_B &= \frac{P}{\sigma_B^2} |\mathbf{h}_B^H \mathbf{w}|^2 = \frac{P}{\sigma_B^2} \sum_{m=1}^M |\mathbf{h}_{B,m}|^2 \\ &= \frac{P}{\sigma_B^2} L_G(R_1)L_H(R_B) \sum_{m=1}^M \left| \sum_{n=1}^N e^{j\phi_n} e^{-j2\pi(f_0 + \Delta f_m)\tilde{\tau}_n^B} \right|^2. \end{aligned}$$

Here, it is noted that the optimal RIS phase shift ϕ_n should be designed to mitigate the term $2\pi(f_0 + \Delta f_m)\tilde{\tau}_n^B$. However, given our assumption of a frequency-flat configuration at the RIS, it is impossible to find a closed-form solution for the optimal phase shift to fully mitigate this term. Therefore, we design the phase shift at the RIS as

$$\phi_n^{\text{opt}} = 2\pi f_0 \tilde{\tau}_n^B, \quad (16)$$

with which the SNR at Bob is computed as

$$\begin{aligned} \gamma_B &= \frac{P}{\sigma_B^2} L_G(R_1)L_H(R_B) \sum_{m=1}^M \left| \sum_{n=1}^N e^{j\phi_n^{\text{opt}}} e^{-j2\pi(f_0 + \Delta f_m)\tilde{\tau}_n^B} \right|^2 \\ &\leq \frac{P}{\sigma_B^2} L_G(R_1)L_H(R_B)MN^2. \end{aligned} \quad (17)$$

The upper bound is achieved when $\Delta f_m = 0$. In fact, as we assume a far-field scenario and $\Delta f_m \ll f_0$, the term $2\pi\Delta f_m\tilde{\tau}_n^B$ is significantly smaller compared to $2\pi f_0\tilde{\tau}_n^B$. Consequently, the gap between the upper bound and γ_B , when employing ϕ_n^{opt} , becomes almost imperceptible. As a closed-form solution leads to tractable secrecy performance and has significantly lower complexity compared to the SDR technique, we utilize the closed-form solution of the RIS for the remainder of the work.

B. Random inverted transmit beamforming and reflective element subset selection (RIBES)

By employing the conventional MRT beamforming in (10) and the RIS configuration proposed in (16), we can effectively improve the received SNR at Bob, consequently leading to an enhancement in the secrecy rate. However, the existence of high-energy signal powers in the proximity of Bob or the RIS may provide an opportunity for a sensitive eavesdropper to correctly decode the transmitted symbols [49]. To address this concern, we utilize RIBES with FDA, where subsets of the transmit antennas and reflective elements are jointly selected at each symbol interval to execute the conventional MRT beamforming and RIS configuration proposed in (10) and (16), respectively. Simultaneously, inverted transmit beamforming and inverted RIS configuration are performed on the remaining subset of the transmit antennas and reflective elements, respectively. More specifically, a subset of the antenna indices, i.e., $\{1, \dots, M\}$, with a size of M_s , is randomly selected at each transmit symbol. In addition, we use $\mathcal{M}_s(k)$ to denote selected subset of the antenna indices. In this context, the transmit beamforming is given by

$$\mathbf{w}^*(k) = \frac{\mathbf{h}_B^*(k)}{\|\mathbf{h}_B^*(k)\|} \circ \mathbf{a}(k), \quad (18)$$

where $\mathbf{a}(k)$ is a M -dimensional vector with $a_m(k) = 1$ if $m \in \mathcal{M}_s(k)$, otherwise $a_m(k) = -1$. Further, $\mathbf{h}_B^*(k)$ in (18) represents the cascaded channel of Bob with RIBES. Meanwhile, the phase shifts at the RIS are hereby configured as

$$\phi_n^*(k) = \begin{cases} 2\pi f_0 \tilde{\tau}_n^B, & \text{if } n \in \mathcal{N}_s(k), \\ 2\pi f_0 \tilde{\tau}_n^B + \pi, & \text{otherwise.} \end{cases} \quad (19)$$

Thereby, $\mathcal{N}_s(k)$ is the selected subset of reflective element indices with a size of N_s . Note that utilizing beamforming improves the strength of the received signal, while employing inverted beamforming degrades it. To ensure that Bob can always benefit from transmit beamforming and RIS, we specify $M_s > M - M_s$ and $N_s > N - N_s$, i.e., $M_s > \frac{M}{2}$ and $N_s > \frac{N}{2}$. By applying FDA and RIBES, we observe the following lemma.

Lemma 1. *The received SNR at Bob with RIBES is given by*

$$\gamma_B^* = \frac{P}{\sigma_B^2} L_G(R_1) L_H(R_B) \frac{(2M_s - M)^2}{M} (2N_s - N)^2. \quad (20)$$

Proof. The proof is provided in Appendix A. \square

Remark 1. *When comparing (17) and (20), we observe that the received SNR at Bob is reduced if RIBES is employed. Nevertheless, the use of RIBES randomizes the received signal at Eve, significantly degrading the received SNR at Eve, as we will see in the next section. Consequently, the secrecy performance can be enhanced.*

IV. SECRECY ANALYSIS

In this section, we first define the scaling factor of the received signal using FDA and RIBES, and then derive its statistical properties. Afterward, we examine the secrecy performance when employing FDA without RIBES. We demonstrate the advantages of utilizing FDA over traditional phased array while also highlighting the associated issues. Subsequently, we delve into an analysis of the secrecy rate when both FDA and RIBES are employed, and show how this approach resolves the issues in the utilization of FDA.

A. Statistical properties of the scaling factor

It is noted that we work within a two dimensional geometric framework, where the positions of the BS and RIS remain fixed. As a result, the user's location can be specified using the parameter tuple (R_{UE}, θ_{UE}) , where R_{UE} is the distance between the RIS and user, and θ_{UE} is the AOA at the receiver, as introduced in Sec. II. With FDA and RIBES, the received signal of Eve with (R_E, θ_E) is

$$\begin{aligned} y_E^*(k) &= \sqrt{P} \mathbf{h}_E^*(k)^H \mathbf{w}^*(k) x(k) + n_E(k) \\ &= \sqrt{\frac{P L_G(R_1) L_H(R_E)}{M}} u(k) v(k) x(k) + n_E(k), \end{aligned} \quad (21)$$

where

$$\begin{aligned} u(k) &= \sum_{m \in \mathcal{M}_s(k)} e^{j2\pi \Delta f_m \frac{R_E - R_B}{c}} - \sum_{m \notin \mathcal{M}_s(k)} e^{j2\pi \Delta f_m \frac{R_E - R_B}{c}}, \\ v(k) &= \sum_{n \in \mathcal{N}_s(k)} e^{j2\pi f_0 (\tilde{\tau}_n^E - \tilde{\tau}_n^B)} - \sum_{n \notin \mathcal{N}_s(k)} e^{j2\pi f_0 (\tilde{\tau}_n^E - \tilde{\tau}_n^B)}. \end{aligned}$$

Due to the randomness of the selected subset $\mathcal{M}_s(k)$ and $\mathcal{N}_s(k)$, both $u(k)$ and $v(k)$ can be treated as random variables for Eve. It is important to note that for the legitimate receiver, Bob, $u(k) = 2M_s - M$ and $v(k) = 2N_s - N$ are constants throughout the transmission. Consequently, the randomness introduced by subset selection has no impact on Bob. For the sake of readability and clarity, we omit the index k in the remaining part of this work. Let us define $\beta(R_E, \theta_E)$ as a scaling factor of the received signal, and it is given by

$$\beta(R_E, \theta_E) = \sqrt{\frac{L_G(R_1) L_H(R_E)}{M}} uv, \quad (22)$$

with which the received signal at Eve in (21) can be rewritten as

$$y_E^* = \sqrt{P} \beta(R_E, \theta_E) x + n_E. \quad (23)$$

Here, we can see that $\beta(R_E, \theta_E)$ is a complex-valued random variable.

Remark 2. *Assuming we have $M = 21$ BS antennas and $N = 21$ reflective elements, for each symbol interval, we randomly select $M_s = 12$ antennas and $N_s = 12$ elements. This results in a total of $\binom{N}{N_s} \binom{M}{M_s} = 293,930^2$ possible combinations of β at each transmit symbol. The extensive number of combinations makes it challenging for an eavesdropper to decode the transmitted symbol. Therefore, the secrecy performance can be enhanced through the use of RIBES.*

In the following lemma, we characterize the statistical properties of $\beta(R_E, \theta_E)$ that are important for the analysis of secrecy performance.

Lemma 2. *The mean of the scaling factor $\beta(R_E, \theta_E)$, when employing FDA and RIBES combined, is*

$$\begin{aligned} \mathbb{E}[\beta(R_E, \theta_E)] & \\ &= \sqrt{\frac{L_G(R_1) L_H(R_E)}{M} \frac{(2M_s - M)(2N_s - N)}{MN}} \mu_1 \mu_2 \mu_3, \end{aligned} \quad (24)$$

where

$$\mu_1 = \frac{\sin(M\pi \Delta F (R_E - R_B)/c)}{\sin(\pi \Delta F (R_E - R_B)/c)}, \quad (25)$$

$$\mu_2 = \frac{\sin(0.5N_H \pi (\cos(\theta_B) - \cos(\theta_E)))}{\sin(0.5\pi (\cos(\theta_B) - \cos(\theta_E)))}, \quad (26)$$

$$\mu_3 = \frac{\sin(0.5N_V \pi (\sin(\theta_E) - \sin(\theta_B)))}{\sin(0.5\pi (\sin(\theta_E) - \sin(\theta_B)))}. \quad (27)$$

The variance of $\beta(R_E, \theta_E)$ is

$$\begin{aligned} \mathbb{V}[\beta(R_E, \theta_E)] & \\ &= \frac{L_G(R_1) L_H(R_E)}{M} (\mathbb{V}[u] \mathbb{V}[v] + \mathbb{V}[v] |\mathbb{E}[u]|^2 + \mathbb{V}[u] |\mathbb{E}[v]|^2), \end{aligned} \quad (28)$$

where

$$\mathbb{E}[u] = \frac{2M_s - M}{M} \mu_1, \quad \mathbb{E}[v] = \frac{2N_s - N}{N} \mu_2 \mu_3, \quad (29)$$

$$\mathbb{V}[u] = 4 \frac{M_s(M - M_s)}{M(M - 1)} \left(M - \frac{1}{M} \mu_1^2 \right), \quad (30)$$

$$\mathbb{V}[v] = 4 \frac{N_s(N - N_s)}{N(N - 1)} \left(N - \frac{1}{N} \mu_2^2 \mu_3^2 \right). \quad (31)$$

Proof. The proof is provided in Appendix B. \square

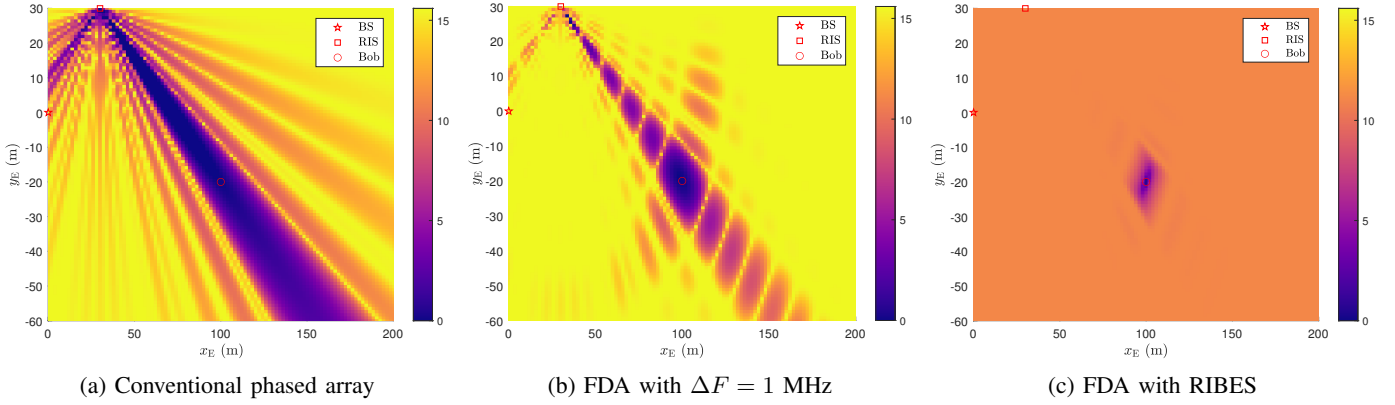


Fig. 2: The heatmaps of the secrecy rate observed when Eve is positioned at $[x_E, y_E]$ using various transmission techniques

B. Secrecy rate with FDA and RIBES

Next, we investigate the secrecy rate with FDA but without RIBES.

Proposition 1. For any eavesdropper with the parameter tuple (R_E, θ_E) , the secrecy rate with FDA is given by

$$C_s(R_E, \theta_E) = \left[\log_2 \left(1 + \frac{P}{\sigma_B^2} L_G(R_1) L_H(R_B) M N^2 \right) - \log_2 \left(1 + \frac{P}{\sigma_E^2} L_G(R_1) L_H(R_E) \frac{\mu_1^2 \mu_2^2 \mu_3^2}{M} \right) \right]^+. \quad (32)$$

Proof. If RIBES is not utilized, the variance of the scaling factor $\beta(R_E, \theta_E)$ becomes zero. Consequently, $\beta(R_E, \theta_E)$ is a constant and can be calculated by employing (24) while setting $M_s = M$ and $N_s = N$. Thus, the received SNR at Eve can be approximated as

$$\gamma_E = \frac{P}{\sigma_E^2} |\beta(R_E, \theta_E)|^2 = \frac{P}{\sigma_E^2} L_G(R_1) L_H(R_E) \frac{\mu_1^2 \mu_2^2 \mu_3^2}{M}.$$

Furthermore, the received SNR at Bob without RIBES, i.e., γ_B , has been approximated in (17). By substituting γ_B and γ_E into (9), we observe the secrecy rate without RIBES. This completes the proof. \square

We know that the maximum value of $\mu_1^2 \mu_2^2 \mu_3^2$ is $M^2 N_H^2 N_V^2$ achieved when $(R_E, \theta_E) = (R_B, \theta_B)$. Thus, the highest SNR at Eve is achieved when their position is identical to Bob. This observation signifies that, with FDA at the transmitter, we can ensure secure transmission within a range that takes both direction and distance into account.

Remark 3. When a conventional phased array is employed at the BS, the secrecy rate is given by

$$C_s^{conv}(\theta_E) = \left[\log_2 \left(1 + \frac{P}{\sigma_B^2} L_G(R_1) L_H(R_B) M N^2 \right) - \log_2 \left(1 + \frac{P}{\sigma_E^2} L_G(R_1) L_H(R_E) M \mu_2^2 \mu_3^2 \right) \right]^+. \quad (33)$$

This term holds because μ_1 equals to M , if $\Delta F = 0$, according to (25). As a result, the secrecy rate with conventional phased array is only direction-dependent, indicating that secure transmission is not possible if Eve is in the same direction as Bob and closer to the RIS.

Here, we demonstrate that a direction-range secured communication can be achieved through the joint use of FDA, MRT transmit beamforming and RIS configuration, as proposed in Sec. III-A. However, there are still certain issues that need to be addressed. The scaling factor $\beta(R_E, \theta_E)$ remains constant and increases linearly with the channel gain. An eavesdropper with a strong channel gain or very low receiver noise might have the potential to successfully decode the transmitted symbol. To tackle this issue, we apply RIBES in this work combined with FDA.

We now analyze the secrecy rate when RIBES is applied. Following (23) and applying Lemma 2, the SNR observed at Eve can be computed as [38]

$$\gamma_E^* = \frac{P |\mathbb{E}[\beta(R_E, \theta_E)]|^2}{P \mathbb{V}[\beta(R_E, \theta_E)] + \sigma_E^2}. \quad (34)$$

Thereby, the closed-form of the secrecy rate with FDA and RIBES can be observed by

$$C_s^*(R_E, \theta_E) = \log_2(1 + \gamma_B^*) - \log_2(1 + \gamma_E^*), \quad (35)$$

where γ_B^* and γ_E^* are stated in (20) and (34), respectively. Note that when the channel gain of Eve grows asymptotically high or the receiver noise at Eve is sufficiently low, such that σ_E^2 in (34) can be ignored, the received SNR at Eve becomes

$$\gamma_E^* \rightarrow \frac{(2M_s - M)^2 (2N_s - N)^2 \mu_1^2 \mu_2^2 \mu_3^2}{M^2 N^2 (\mathbb{V}[u] \mathbb{V}[v] + \mathbb{V}[v] |\mathbb{E}[u]|^2 + \mathbb{V}[u] |\mathbb{E}[v]|^2)}. \quad (36)$$

This equation holds because the numerator and denominator of γ_E^* in (34) both linearly depend on the term of $L_G(R_1) L_H(R_E)$, according to Lemma 2. Consequently, the secrecy rate remains unaffected by the eavesdropper's channel gain. It is thus shown that RIBES is robust to high channel gains and low receiver noise at eavesdroppers.

Example: We show an illustration of the secrecy rate observed at coordinates $[x_E, y_E]$ when applying various transmission techniques in Fig. 2. The BS, RIS, and the target receiver Bob are located at $[0 \text{ m}, 0 \text{ m}]$, $[30 \text{ m}, 30 \text{ m}]$, and $[100 \text{ m}, -20 \text{ m}]$, respectively. Furthermore, we set $M = 21$, $N_H = N_V = 21$, $P = 30 \text{ dBm}$, $\sigma_B^2 = \sigma_E^2 = -120 \text{ dBm}$. Fig. 2a illustrates the secrecy rate when a conventional phased array is employed. We observe that the main beam is directed toward the target receiver Bob, and within the main beam

region, the secrecy rate is very low. Notably, when Eve is positioned closer to the RIS than Bob, the secrecy rate within the main beam region drops to zero due to Eve's higher SNR compared to Bob. Fig. 2b shows the secrecy rate for the case that FDA are used with a fixed frequency increment of $\Delta F = 1$ MHz. In this figure, we observe that a positive secrecy rate can be achieved when Eve is positioned in the same direction as Bob and is closer to the RIS. However, multiple local minima of the secrecy rate are present due to high energy leakage on the side lobes. Furthermore, when Eve is in close proximity to the RIS, the secrecy rate drops to zero due to Eve's significantly higher channel gain compared to Bob. These issues can be addressed by applying both FDA and RIBES, as shown in Fig. 2c. In this case, the overall secrecy performance is significantly enhanced compared to Fig. 2a and Fig. 2b. A global minimum of the secrecy rate is observed when Eve is at the exact same location as Bob. Furthermore, the secrecy rate observed for the case that Eve is in the proximity of Bob or RIS is improved. However, the maximal secrecy rate is around 10.5 bits/sec/Hz only, which is lower than the maximal secrecy rate of 15 bits/sec/Hz observed in Fig. 2a and Fig. 2b. This is because the random subset selection randomizes the received signal at Eve, but also reduces the received signal power at Bob. In fact, there is a trade-off between the SNR at Bob and Eve with respect to M_s and N_s . Hence, M_s and N_s are optimized to maximize the secrecy rate in the following section.

V. SECRECY RATE OPTIMIZATION

If no prior information about Eve's location is given, it is challenging to find the optimal subset sizes of the transmit antennas and reflective elements that maximize the secrecy rate. To address this challenge, we define the wiretap area for our setup. Under the assumption that the eavesdropper is located within the wiretap area, we derive the *worst-case secrecy rate*, which is optimized by determining the optimal value of M_s and N_s . Furthermore, we optimize the frequency increment at the BS when the eavesdropper's location is given, and derive the upper bound for the secrecy rate.

A. Optimization without information of Eve's location

We now define the wiretap area for our setup, the boundary of which is determined by the first null point of the received SNR at Eve. From Lemma 2 and (34), we can see that the null points of the received SNR at Eve with respect to R_E are determined by the null points of μ_1 , while the null points with respect to θ_E is same as the null points of $\mu_2\mu_3$. From [50], the null points of μ_1 occur when

$$\begin{aligned} 2\pi M \Delta F \frac{R_E - R_B}{c} &= \pm 2i\pi, \\ \text{s.t. } i &\neq kM, \quad i \in \mathbb{Z}^+, \quad k \in \mathbb{Z}^+ \end{aligned} \quad (37)$$

holds. We observe the first null of the received SNR at Eve is achieved when $|R_E - R_B| = \Delta R = \frac{c}{M\Delta F}$. Similarly, the null points of μ_2 occur when

$$\begin{aligned} N_H \pi (\cos \theta_B - \cos \theta_E) &= \pm 2i\pi, \\ \text{s.t. } i &\neq kN_H, \quad i \in \mathbb{Z}^+, \quad k \in \mathbb{Z}^+ \end{aligned} \quad (38)$$

holds. Hence the first null of μ_2 is obtained when $\theta_E = \arccos(\cos \theta_B \pm \frac{2}{N_H})$, indicating that we have

$$|\theta_E - \theta_B| = \Delta\theta_1 = \left| \arccos \left(\cos \theta_B \pm \frac{2}{N_H} \right) - \theta_B \right|.$$

Similarly, the first null of μ_3 is obtained when

$$|\theta_E - \theta_B| = \Delta\theta_2 = \left| \arcsin \left(\sin \theta_B \pm \frac{2}{N_V} \right) - \theta_B \right|.$$

As the received SNR at Eve is determined by the product of μ_2 and μ_3 , the first null of Eve's received SNR concerning θ_E is determined by $\min(\Delta\theta_1, \Delta\theta_2)$. Thus, the wiretap area and the corresponding target area are defined as follows.

Definition 1. *The wiretap area in an RIS-assisted mmWave/THz transmission with FDA is*

$$\mathcal{R} = \left\{ (R_E, \theta_E) \mid |R_E - R_B| \geq \Delta R, \right. \\ \left. |\theta_E - \theta_B| \geq \min(\Delta\theta_1, \Delta\theta_2) \right\}, \quad (39)$$

where ΔR , $\Delta\theta_1$ and $\Delta\theta_2$ are, respectively, given by

$$\begin{aligned} \Delta R &= \frac{c}{M\Delta F}, \\ \Delta\theta_1 &= \left| \arccos \left(\cos \theta_B \pm \frac{2}{N_H} \right) - \theta_B \right|, \\ \Delta\theta_2 &= \left| \arcsin \left(\sin \theta_B \pm \frac{2}{N_V} \right) - \theta_B \right|. \end{aligned} \quad (40)$$

Definition 2. *The complementary set of the wiretap area \mathcal{R} defines the target area.*

Remark 4. *The size of the target area decreases with the increasing number of transmit antennas and reflective elements, indicating a more focused transmission. Within the target area, the received SNR at Eve reaches its maximum when Eve is in the same position as Bob, and decreases with an increasing distance. Furthermore, in the target area, the channel gains of Bob and Eve are nearly identical. Therefore, it is reasonable to assume that a secure transmission can always be achieved if the eavesdropper is in the wiretap area.*

In this work, we assume that the eavesdropper is located in the wiretap area. Under this assumption, the *worst-case secrecy rate* can be expressed as

$$C_s^{\text{w-c}} = \log_2(1 + \gamma_B^*) - \max_{(\theta_E, R_E) \in \mathcal{R}} \log_2(1 + \gamma_E^*). \quad (41)$$

It is noticed that there is a trade-off between the first part and the second part of (41) when RIBES is applied. Given that we assume $M_s > \frac{M}{2}$ and $N_s > \frac{N}{2}$, when M_s and N_s increase, the rate at Bob, i.e., $\log_2(1 + \gamma_B^*)$, also increases, while the negative rate at Eve, i.e., $-\log_2(1 + \gamma_E^*)$, decreases. The reason is that the randomness of the subset selection is maximized when exactly half of the transmit antennas and half of the reflective elements are chosen, as the maximal value of $\binom{N}{N_s} \binom{M}{M_s}$ is achieved when $N_s = \frac{N}{2}$ and $M_s = \frac{M}{2}$. As a result, $-\log_2(1 + \gamma_E^*)$ achieves its maximum when $N_s = \frac{N}{2}$ and $M_s = \frac{M}{2}$. Therefore, in the following we aim to determine

the optimal values of M_s and N_s that maximize the *worst-case secrecy rate*. Hence, the problem of interest is formulated as

$$\max_{M_s, N_s} C_s^{\text{W-C}}(M_s, N_s). \quad (42)$$

To solve this problem, we now derive the upper bound of the received SNR at Eve.

Lemma 3. *With FDA and RIBES, and for any eavesdropper within the wiretap area, we observe*

$$\gamma_E^* \leq \gamma_E^{\text{UB},1} = \frac{(2M_s - M)^2(M - 1)}{4M_s(M - M_s)(M^2 \sin^2(\frac{3\pi}{2M}) - 1)}, \theta_E = \theta_B, \quad (43)$$

$$\gamma_E^* \leq \gamma_E^{\text{UB},2} = \frac{(2N_s - N)^2(N - 1)\lambda^2}{4N_s(N - N_s)(N^2 - \lambda^2)}, R_E = R_B, \quad (44)$$

where λ is the maximum of $\mu_2\mu_3$ in the wiretap area, and it can be approximated by

$$\lambda \approx \max \left(\frac{\sin(N_V \Lambda_H)}{\sin(\frac{3\pi}{2N_H}) \sin(\Lambda_H)}, \frac{\sin(N_H \Lambda_V)}{\sin(\frac{3\pi}{2N_V}) \sin(\Lambda_V)} \right), \quad (45)$$

$$\text{where } \Lambda_H = 0.5\pi \left(\sqrt{1 - \left(\cos \theta_B \pm \frac{3}{N_H} \right)^2} - \sin \theta_B \right),$$

$$\Lambda_V = 0.5\pi \left(\cos \theta_B - \sqrt{1 - \left(\sin \theta_B \pm \frac{3}{N_V} \right)^2} \right).$$

Proof. The proof is provided in Appendix C. \square

From Lemma 3, we can see that if $\theta_E = \theta_B$, the upper bound depends only on M and M_s . Also, if $R_E = R_B$, the upper bound is only related to N and N_s . Therefore, we divide the problem in (42) into two sub-problems, expressed as

$$\max_{M_s} \log_2(1 + \gamma_B^*) - \log_2 \left(1 + \gamma_E^{\text{UB},1} \right), \quad (46)$$

$$\max_{N_s} \log_2(1 + \gamma_B^*) - \log_2 \left(1 + \gamma_E^{\text{UB},2} \right), \quad (47)$$

respectively. Here, the objective of (46) can be considered as a function of M_s given N_s . Thus, the optimal value for M_s can be found through the zero of the first derivative of the objective. The solution to (47) can be obtained using a similar approach. Hence, we observe the following theorem.

Theorem 1. *In RIS-assisted secure transmission with FDA and RIBES, the optimal subset size of the selected antennas to maximize the worst-case secrecy rate is*

$$M_s^* = \left\lfloor \frac{M}{2} \left(1 + \sqrt{\frac{1 - \frac{1}{M} \sqrt{\eta_B^{-1} \eta_E (\eta_E - 1) + M^2}}{1 - \eta_E}} \right) \right\rfloor, \quad (48)$$

where $\eta_B = \frac{P}{M\sigma_B^2} L_G(R_1) L_H(R_B) (2N_s - N)^2$ and $\eta_E = \frac{(M-1)}{M^2 \sin^2(\frac{3\pi}{2M}) - 1}$. Furthermore, the optimal subset size of the selected elements is given by

$$N_s^* = \left\lfloor \frac{N}{2} \left(1 + \sqrt{\frac{1 - \frac{1}{N} \sqrt{\zeta_B^{-1} \zeta_E (\zeta_E - 1) + N^2}}{1 - \zeta_E}} \right) \right\rfloor, \quad (49)$$

where $\zeta_B = \frac{P}{M\sigma_B^2} L_G(R_1) L_H(R_B) (2M_s - M)^2$ and $\zeta_E = \frac{(N-1)\lambda^2}{N^2 - \lambda^2}$.

Proof. The proof is provided in Appendix D. \square

Proposition 2. *When γ_B^* is significantly larger than one, i.e., 0 dB, Theorem 1 can be simplified as*

$$M_s^* = \left\lfloor \frac{M}{2} \left(1 + \frac{1}{\sqrt{1 + \sqrt{\eta_E}}} \right) \right\rfloor, \quad (50)$$

$$N_s^* = \left\lfloor \frac{N}{2} \left(1 + \frac{1}{\sqrt{1 + \sqrt{\zeta_E}}} \right) \right\rfloor. \quad (51)$$

Proof. The proposition can be proven similar to the proof provided for Theorem 1 in Appendix C. Thereby, the approximation $1 + \gamma_B^* \approx \gamma_B^*$ is used. \square

From Proposition 2, we can easily determine the optimal subset size of the selected antennas based on M for the case that $\gamma_B^* \gg 0$ dB. For the same case, the optimal subset size of the selected elements is only dependent on N . It is worth noting that $\gamma_B^* \gg 0$ dB holds true in RIS-assisted systems with a sufficiently large number of elements [51]–[53].

B. Optimization given Eve's Location

The secrecy rate can be further enhanced when Eve's location is known at the BS. Assuming that the frequency increments between neighboring antennas can be perfectly adjusted, we can find an optimal frequency increment such that the received SNR of Eve is always $-\infty$ dB. According to (37), the mean value of $\beta(R_E, \theta_E)$ becomes zero, if

$$\Delta F^* = \frac{\pm ic}{M(R_E - R_B)}, \quad \frac{M-1}{2} \Delta F^* \leq 10^{-3} f_0. \quad (52)$$

Consequently, the received SNR at Eve is $-\infty$ dB. In this context, the achievable secrecy rate is equivalent to the communication rate at Bob, i.e.,

$$C_s^* = \log_2(1 + \gamma_B^*) = \log_2 \left(1 + \frac{P}{\sigma_B^2} L_G(R_1) L_H(R_B) \times \frac{(2M_s - M)^2}{M} (2N_s - N)^2 \right). \quad (53)$$

Note that, for the case that Eve's location is known and the optimally designed frequency increment is employed, the maximal secrecy rate will be achieved if $M_s = M$ and $N_s = N$, indicating that RIBES does not need to be employed. Then, the secrecy rate becomes

$$C_s^{\text{UB}} = \log_2 \left(1 + \frac{P}{\sigma_B^2} L_G(R_1) L_H(R_B) M N^2 \right). \quad (54)$$

Note that, achieving a perfect frequency increment is not always possible due to hardware limitations and the constraint of the maximum frequency increment, i.e., $\max(\Delta F_m) < 10^{-3} f_0$. Nevertheless, (54) is still an upper bound of the secrecy rate.

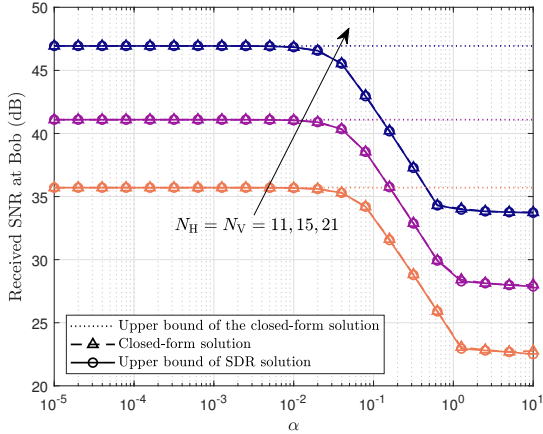


Fig. 3: Comparison of received SNR at Bob using different RIS solutions with various number of reflective elements

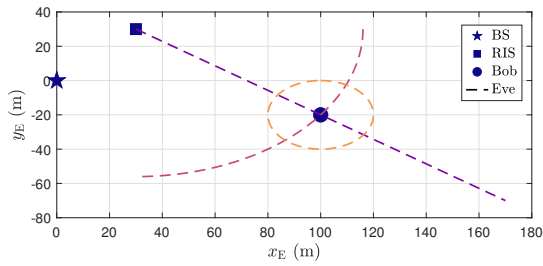


Fig. 4: Considered locations of all devices. Dashed lines: potential locations of Eve

VI. NUMERICAL RESULTS

In this section, we present the numerical results associated with the analytical results derived in this work. Throughout the simulations, we set $P = 30$ dBm, $\sigma_B^2 = \sigma_E^2 = -120$ dBm. The path loss of the mmWave/THz channel is modeled as $L(R) = L_0 + 10\alpha \log_{10}(R)$ [dB], where R , L_0 and α are the propagation distance, path loss value at a reference distance of 1 m, and path loss exponent. Here, we employ a large reference path loss $L_0 = 60$ dB to align with the propagation conditions of mmWave/THz. Additionally, we set α to 2. The center frequency is $f_0 = 60$ GHz. Moreover, the BS, RIS and Bob are located at $[0 \text{ m}, 0 \text{ m}]$, $[30 \text{ m}, 30 \text{ m}]$, and $[100 \text{ m}, -20 \text{ m}]$, respectively. From this parameter choice follows that $\theta_B = 0.62$ rad and $R_B = 86.02$ m.

We first evaluate the performance of the proposed closed-form solution of ϕ_n^{opt} stated in (16) in terms of the received SNR at Bob. In Fig. 3, we compare the accurate simulation results using the closed-form solution with the upper bound in (17), and the upper bound obtained by solving the SDR problem in (12). The SNR is presented over $\alpha = \frac{\max(\Delta F_m)}{f_0}$, i.e., the ratio of the maximal frequency shift and the center frequency. From this figure, we observe that the results obtained using the closed-form solution almost align with the upper bound achieved through SDR. Additionally, the performance gap between the upper bound of the closed-form solution and the accurate simulation result is negligible and can be disregarded when α is less than 10^{-2} . Hence, in the following results, we set $\max(\Delta F_m) < 10^{-3} f_0$.

In the following subsections, we investigate the received SNRs at Bob and Eve and the resulting secrecy rate under the

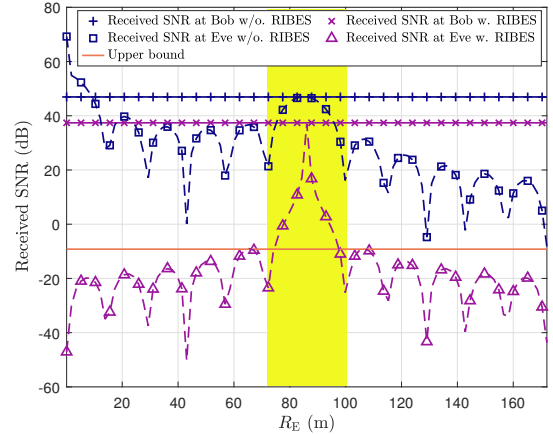


Fig. 5: Comparison of the received SNR at Bob and Eve with different transmission techniques, $M_s = \lfloor \frac{2}{3} M \rfloor$. Markers: simulation results; curves: theoretical results.

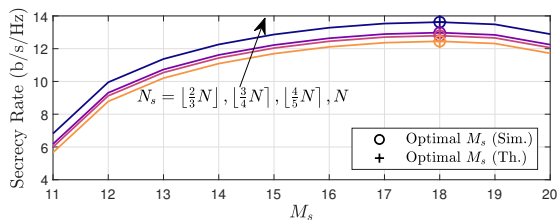
assumption that Eve is located along different, beneficial paths, as depicted in Fig. 4. In more details, first, the case where the AOA at Bob is the same as the one of Eve, i.e., $\theta_B = \theta_E$, is investigated (purple path). Second, Bob and Eve are assumed to be located equidistant from the RIS, i.e., $R_B = R_E$, (red path). Finally, a scenario is considered where Eve is located on a circle centered at Bob (orange path). In these scenarios, we set $M = N_H = N_V = 21$ and $\Delta F = 1$ MHz (if not specified otherwise).

A. Equal AOA at Bob and Eve

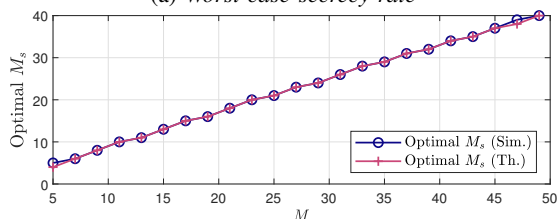
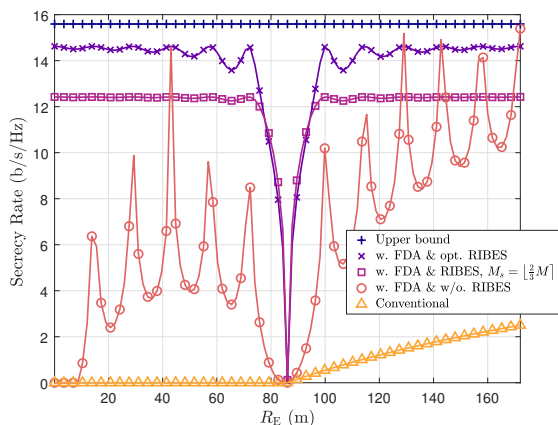
We now examine the performance of the proposed transmission technique when $\theta_B = \theta_E$. In this case, according to Lemma 2, random elements subset selection at the RIS does not provide any benefit. Thus, we set $N_s = N$ (if not specified otherwise).

The received SNR at Bob and Eve with different transmission techniques with respect to R_E is illustrated in Fig. 5. The yellow-shaded area in the middle of the figure (the vertical strip between 71.74 m and 100.31 m) shows the target area, according to Definition 2. The perfect match between the curves and markers in this figure indicates the correctness of the closed-form expressions. Further, we observe that the received SNR at Bob is slightly reduced when RIBES is applied, while the received SNR at Eve is significantly degraded, especially in the wiretap area. In addition, as R_E decreases, the peaks of the received SNR at Eve increase for the case that RIBES is not employed. In particular, without RIBES and when R_E is less than 10 m, the received SNR at Eve exceeds that at Bob. This is because the channel gain of Eve is significantly larger than that of Bob. However, when RIBES is applied, we observe that the values of the peaks decrease with decreasing R_E . As a result, Eve always has a lower SNR than Bob, indicating secure transmission can be achieved. We also plot the upper bound computed by (43) in Lemma 3, which agrees well with the maximum received SNR at Eve in the wiretap area when RIBES is applied.

Fig. 6a illustrates the *worst-case secrecy rate* over the parameter M_s when Eve is positioned within the wiretap area. Moreover, we compare the optimal value of M_s that maximizes the *worst-case secrecy rate* obtained through simulation

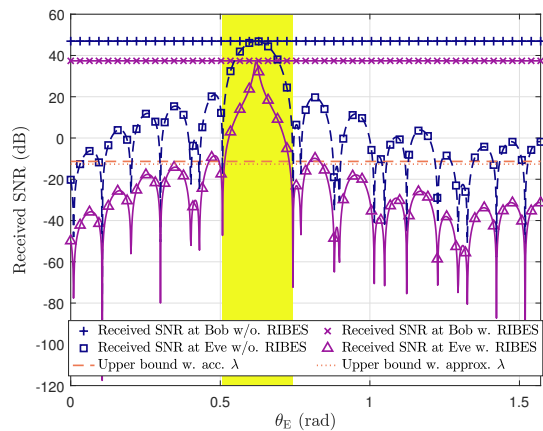


(a) Worst-case secrecy rate

(b) Optimal M_s with various M , $N_s = N$ Fig. 6: Performance of the optimized RIBES, $\theta_B = \theta_E$ Fig. 7: Secrecy rate with respect to R_E . Markers: simulation results; curves: theoretical results.

and the theoretical optimal value obtained by (48) in Theorem 1. The perfect match between the two indicates that (48) in Theorem 1 is accurate. Furthermore, it is noteworthy that the optimal value of M_s does not depend on the value of N_s in these results. This is due to the fact that the received SNR at Bob is significantly larger 0 dB, rendering the optimal value of M_s independent of N_s (as per Proposition 2). In addition, we present the optimal M_s as a function of M in Fig. 6b. The figure shows that the optimal M_s computed by (48) in Theorem 1, closely matches the results obtained through simulation with varying M .

In Fig. 7, we illustrate the secrecy rate as a function of R_E . Thereby, the results of different transmission techniques are compared, including the employment of a conventional phased array at the BS, using FDA at the BS without RIBES, leveraging FDA and RIBES jointly with $M_s = \lfloor \frac{2}{3}M \rfloor$, and using FDA along with optimized RIBES. From this figure, we can observe that the simulation results align with the analytical results, verifying the accuracy of the closed-form expressions derived in Sec. IV. Furthermore, when $R_E < R_B$, the secrecy rate is zero when a conventional phased array is employed. However, when employing FDA without RIBES, a positive secrecy rate can be achieved, in cases where $R_E > 10$ m. Further, when FDA and RIBES are applied jointly, we observe

Fig. 8: Comparison of the received SNR at Bob and Eve with different transmission techniques, $N_s = \lfloor \frac{2}{3}N \rfloor$ and $M_s = M$. Markers: simulation results; curves: theoretical results.

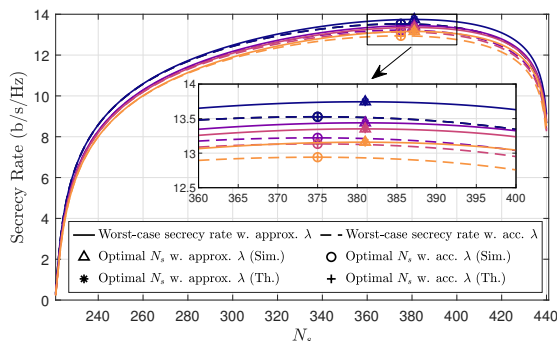
a high secrecy rate even if Eve is at a very short distance from the RIS. This demonstrates the robustness of RIBES against high channel gain at Eve. Additionally, when Eve is in proximity to Bob, the secrecy rate achieved with both FDA and RIBES surpasses the secrecy rate obtained when only FDA is applied. Moreover, we see that the secrecy performance can be enhanced when optimized RIBES is applied. It is noted that we also observe a higher secrecy rate without RIBES compared to with RIBES at a few specific values of R_E . This is because, at these specific values, the eavesdropper is either close to or positioned at the null points. In such cases, the upper bound of the secrecy rate specified in (54) is achieved at the null points without RIBES.

B. Equal distance from the RIS at Bob and Eve

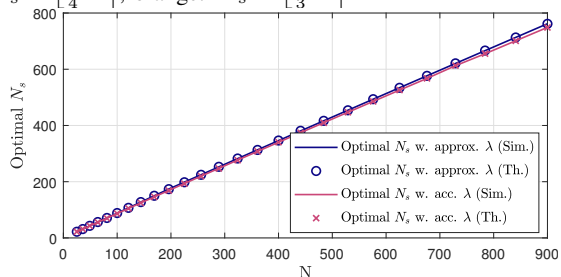
Now, we evaluate the performance of the proposed transmission technique when $R_B = R_E$. Thereby, we set $\Delta F = 0$, since FDA does not confer any advantages. This is because we have $\mathbb{V}[u] = 0$ according to Lemma 2 (30).

In Fig. 8, we compare the received SNR at Bob and Eve with and without RIBES. We observe that the markers align well with the curves, confirming the correctness of the closed-form expressions. Meanwhile, when Eve is located in the target area (indicated with a yellow background), and as the distance between the AOA at Bob and Eve increases, the received SNR at Eve decreases more rapidly with RIBES than without it. In addition, we compare the upper bound of the received SNR at Eve in the wiretap area when using the accurate λ and the approximate λ observed by (45) in Lemma 2. Here, the accurate λ is observed by simulations. The corresponding curves show that there is only a slight difference between the upper bounds computed by accurate and approximate λ . Therefore, it is reasonable to utilize the approximate upper bound for determining the optimal value of N_s .

Now, we illustrate the *worst-case secrecy rate* in the wiretap area as a function of N_s in Fig. 9a. In particular, we compare the upper bound with approximate and accurate λ , where we observe a minor gap between them. Nevertheless, these two bounds exhibit a similar behavior across various values of N_s . In addition, the value of N_s optimized using the approximate



(a) Worst-case secrecy rate. Blue: $M_s = M$; purple: $M_s = \lfloor \frac{3}{4} M \rfloor$; red: $M_s = \lfloor \frac{2}{3} M \rfloor$



(b) Optimal N_s with various N , $M_s = M$

Fig. 9: Performance of the optimized RIBES, $R_B = R_E$

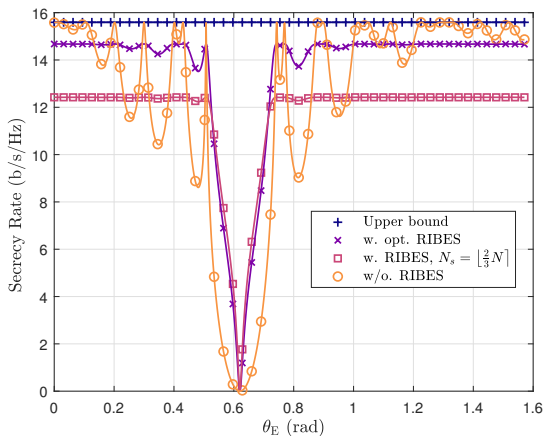


Fig. 10: Secrecy rate as a function of θ_E , $M_s = M$. Markers: simulation results; curves: theoretical results.

λ is close to that using accurate λ . This can be observed from Fig. 9b, where we plot the optimal N_s as function of N . In both figures, we observe a perfect match between the optimal N_s obtained through simulation and the closed-form expression in (51), which verifies the validity of Theorem 1. Meanwhile, from Fig. 9a, the optimal N_s remains unchanged across different values of M_s due to the fact that $\gamma_B^* \gg 1$ (as seen in Proposition 2).

In Fig. 10, we plot the secrecy rate as a function of θ_E . It can be observed that when Eve is located close to Bob, i.e., when the distance in the AOA between Bob and Eve is small, the secrecy performance with RIBES significantly outperforms that without RIBES. As this distance increases, the secrecy rate with RIBES converges to a constant, while the secrecy rate without RIBES remains dependent on the AOA. Meanwhile, at some specific values of θ_E , the secrecy rate without RIBES is higher than with RIBES. This occurs

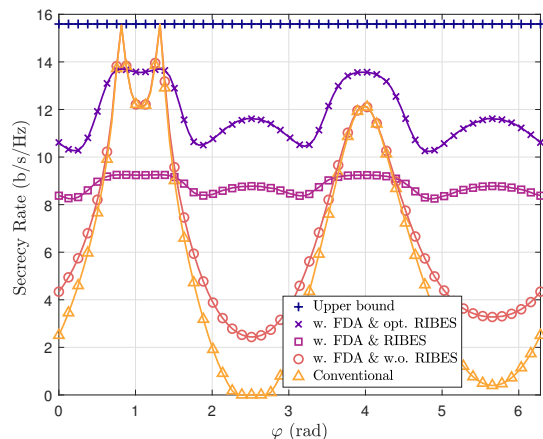


Fig. 11: Secrecy rate with $D = 10$ m. Markers: simulation results; curves: theoretical results.

because the received SNR at Eve is close to or equals zero at these particular values, and the upper bound of the secrecy rate is achieved when RIBES is not employed according to (54). Furthermore, it is evident that optimizing the RIBES can enhance the secrecy rate and generally results in a better overall performance compared to not using RIBES.

C. Eve on a circle around Bob

We now examine the secrecy rate when Eve is located with a fixed distance to Bob. In this case, the locations of Eve can be determined by $x_E = x_B + D \cos \varphi$ and $y_E = y_B + D \sin \varphi$, for $\varphi \in [0, 2\pi]$, where D is the radius of the trajectory. In Fig. 11, we depict the secrecy rate as a function of φ . It is evident that the markers closely match the curves, which once again verifies the accuracy of the closed-form expressions. In addition, we can see that when φ ranges between 2 and 3 radians, a zero secrecy rate is obtained when conventional phases array is applied. This is because in this range, Eve is almost aligned with Bob ($\theta_B \approx \theta_E$) and Eve is closer to the RIS than Bob. When FDA is utilized, a positive secrecy rate can be always achieved. However, we still observe a low secrecy rate when Eve is located in the same direction as Bob without RIBES. From this figure, we can see that the utilization of RIBES enhances the secrecy rate, especially when Eve is aligned with Bob. Furthermore, the proposed optimized RIBES can effectively improve the secrecy rate.

VII. CONCLUSION

In this work, we have proposed FDA with RIBES to enable secure communication in an RIS-assisted mmWave/THz communication system, providing both direction and range protection. Specifically, we have considered a passive eavesdropper and designed the transmit beamforming and RIS configuration based on Bob's channel information. We have further derived closed-form expressions for the secrecy rate using the proposed algorithms, and these results were validated through extensive simulations. Additionally, the *worst-case secrecy rate* has been analyzed for the case that Eve is located in the wiretap area. Furthermore, we have determined the optimal subset sizes of the selected transmit antennas and reflective elements in closed form. Numerical results demonstrate that

the proposed algorithm provides an enhanced secrecy rate compared to conventional approaches, particularly when Eve is in the proximity to Bob or the RIS.

APPENDIX

A. Proof of Lemma 1

By substituting (19) in to (13), the cascaded channel of Bob is computed as

$$\begin{aligned} \mathbf{h}_{B,m}^*(k) &= \sqrt{L_G(R_1)L_H(R_B)} e^{-j2\pi f_m \left(\frac{R_1+R_B}{c} + \tilde{\tau}_m\right)} \times \\ &\left(\sum_{n \in \mathcal{N}_s(k)} e^{-j2\pi f_m \tilde{\tau}_n^B} e^{j\phi_n^*(k)} + \sum_{n \notin \mathcal{N}_s(k)} e^{-j2\pi f_m \tilde{\tau}_n^B} e^{j\phi_n^*(k)} \right) \\ &\stackrel{(a)}{=} \sqrt{L_G(R_1)L_H(R_B)} e^{-j2\pi f_m \left(\frac{R_1+R_B}{c} + \tilde{\tau}_m\right)} (N_s - (N - N_s)) \\ &= \sqrt{L_G(R_1)L_H(R_B)} e^{-j2\pi f_m \left(\frac{R_1+R_B}{c} + \tilde{\tau}_m\right)} (2N_s - N), \end{aligned}$$

where (a) holds as $2\pi\Delta f_m \tilde{\tau}_n^B$ is significantly smaller compared to $2\pi\Delta f_0 \tilde{\tau}_n^B$, and thus, it is disregarded. Accordingly, we have $\|\mathbf{h}_{B,m}^*(k)\| = \sqrt{ML_G(R_1)L_H(R_B)}(2N_s - N)$. As a result, the signal received by Bob can be expressed as

$$\begin{aligned} y_B^*(k) &= \sqrt{P}\mathbf{h}_{B,m}^*(k)^H \mathbf{w}^*(k)x(k) + n_B(k) \\ &= \frac{\sqrt{P}x(k)}{\|\mathbf{h}_{B,m}^*(k)\|} \mathbf{h}_{B,m}^*(k)^H (\mathbf{h}_{B,m}^*(k) \circ \mathbf{a}(k)) + n_B(k) \\ &= \frac{\sqrt{P}x(k)}{\|\mathbf{h}_{B,m}^*(k)\|} \left(\sum_{m \in \mathcal{M}_s(k)} |\mathbf{h}_{B,m}^*|^2 - \sum_{m \notin \mathcal{M}_s(k)} |\mathbf{h}_{B,m}^*|^2 \right) + n_B(k) \\ &= \frac{\sqrt{P}x(k)L_G(R_1)L_H(R_B)(2N_s - N)^2}{\sqrt{ML_G(R_1)L_H(R_B)}(2N_s - N)} (2M_s - M) + n_B(k) \\ &= \sqrt{\frac{PL_G(R_1)L_H(R_B)}{M}} (2M_s - M)(2N_s - N)x(k) + n_B(k). \end{aligned}$$

Thereby, the received SNR at Bob with RIBES can be computed as

$$\gamma_B^* = \frac{P}{\sigma_B^2} L_G(R_1)L_H(R_B) \frac{(2M_s - M)^2}{M} (2N_s - N)^2. \quad (55)$$

B. Proof of Lemma 2

As u and v are two independent and uncorrelated parameters, the expectation of the scaling factor is computed by

$$\mathbb{E}[\beta(R_E, \theta_E)] = \sqrt{\frac{L_G(R_1)L_H(R_E)}{M}} \mathbb{E}[u]\mathbb{E}[v]. \quad (56)$$

Further, the mean value of u is calculated as

$$\begin{aligned} \mathbb{E}[u] &= \mathbb{E}\left[2 \sum_{m \in \mathcal{M}_s(k)} e^{j2\pi\Delta f_m \frac{R_E - R_B}{c}} - \sum_{m=1}^M e^{j2\pi\Delta f_m \frac{R_E - R_B}{c}}\right] \\ &= 2\mathbb{E}\left[\sum_{m \in \mathcal{M}_s(k)} e^{j2\pi\Delta f_m \frac{R_E - R_B}{c}}\right] - \sum_{m=1}^M e^{j2\pi\Delta f_m \frac{R_E - R_B}{c}} \\ &\stackrel{(a)}{=} 2\frac{M_s}{M} \sum_{m=1}^M e^{j2\pi\Delta f_m \frac{R_E - R_B}{c}} - \sum_{m=1}^M e^{j2\pi\Delta f_m \frac{R_E - R_B}{c}} \\ &= \frac{2M_s - M}{M} \sum_{m=1}^M e^{j2\pi\Delta f_m \frac{R_E - R_B}{c}} \\ &= \frac{2M_s - M}{M} \frac{e^{-j\pi M \Delta F \frac{R_E - R_B}{c}} - e^{j\pi M \Delta F \frac{R_E - R_B}{c}}}{e^{-j\pi \Delta F \frac{R_E - R_B}{c}} - e^{j\pi \Delta F \frac{R_E - R_B}{c}}} \\ &= \frac{2M_s - M}{M} \underbrace{\frac{\sin(M\pi\Delta F(R_E - R_B)/c)}{\sin(\pi\Delta F(R_E - R_B)/c)}}_{\mu_1}, \end{aligned} \quad (57)$$

where (a) follows the expectation of random sampling without replacement [54]. Similarly, the mean value of v can be computed by

$$\begin{aligned} \mathbb{E}[v] &= 2\mathbb{E}\left[\sum_{n \in \mathcal{N}_s(k)} e^{j2\pi f_0(\tilde{\tau}_n^E - \tilde{\tau}_n^B)}\right] - \sum_{n=1}^N e^{j2\pi f_0(\tilde{\tau}_n^E - \tilde{\tau}_n^B)} \\ &= \frac{2N_s - N}{N} \sum_{n=1}^N e^{j2\pi f_0(\tilde{\tau}_n^E - \tilde{\tau}_n^B)} \\ &= \frac{2N_s - N}{N} \sum_{n_H=1}^{N_H} \sum_{n_V=1}^{N_V} e^{j2\pi f_0(\tilde{\tau}_n^E - \tilde{\tau}_n^B)} \\ &= \frac{2N_s - N}{N} \sum_{n_H=1}^{N_H} e^{j2\pi \frac{f_0}{c} d_H (\cos(\theta_B) - \cos(\theta_E))} (n_H - \frac{N_H+1}{2}) \\ &\quad \times \sum_{n_V=1}^{N_V} e^{j2\pi \frac{f_0}{c} d_V (\sin(\theta_E) - \sin(\theta_B))} (n_V - \frac{N_V+1}{2}) \\ &= \frac{2N_s - N}{N} \underbrace{\frac{\sin(0.5N_H\pi(\cos(\theta_B) - \cos(\theta_E)))}{\sin(0.5\pi(\cos(\theta_B) - \cos(\theta_E)))}}_{\mu_2} \\ &\quad \times \underbrace{\frac{\sin(0.5N_V\pi(\sin(\theta_E) - \sin(\theta_B)))}{\sin(0.5\pi(\sin(\theta_E) - \sin(\theta_B)))}}_{\mu_3}. \end{aligned} \quad (58)$$

By substituting (57) and (58) into (56), we obtain (24) in Lemma 1. Furthermore, for the variance of the scaling factor, we have

$$\begin{aligned} \mathbb{V}[\beta(R_E, \theta_E)] &= \frac{1}{M} L_G(R_1)L_H(R_E) \mathbb{V}[uv] \\ &= \frac{1}{M} L_G(R_1)L_H(R_E) \left(\mathbb{V}[u]\mathbb{V}[v] + \mathbb{V}[v]|\mathbb{E}[u]|^2 + \mathbb{V}[u]|\mathbb{E}[v]|^2 \right). \end{aligned}$$

Given the fact that $\mathbb{V}[x] = \mathbb{E}[x^2] - \mathbb{E}[x]^2$, and let $x = \sum_{m \in \mathcal{M}_s(k)} e^{j2\pi\Delta f_m \frac{R_E - R_B}{c}}$, the variance of u is calculated as

$$\mathbb{V}[u] = 4\mathbb{V}\left[\sum_{m \in \mathcal{M}_s(k)} e^{j2\pi\Delta f_m \frac{R_E - R_B}{c}}\right] = 4(\mathbb{E}[x^2] - \mathbb{E}[x]^2),$$

where we have

$$\begin{aligned} \mathbb{E}[x^2] &= M_s + \frac{M_s - 1}{M - 1} \left(\left(\sum_{m=1}^M e^{j2\pi\Delta f_m \frac{R_E - R_B}{c}} \right)^2 - M \right) \\ &= M_s + \frac{M_s - 1}{M - 1} (\mu_1^2 - M), \end{aligned}$$

and $\mathbb{E}[x^2] = \frac{M_s^2}{M^2} \mu_1^2$. Thereby, we obtain

$$\begin{aligned} \mathbb{V}[u] &= 4 \left(M_s + \frac{M_s - 1}{M - 1} (\mu_1^2 - M) - \frac{M_s^2}{M^2} \mu_1^2 \right) \\ &= 4 \frac{M_s(M - M_s)}{M(M - 1)} \left(M - \frac{1}{M} \mu_1^2 \right). \end{aligned} \quad (59)$$

The variance of v is obtained similarly.

C. Proof of Lemma 3

We first prove the upper bound of the received SNR at Eve when $\theta_E = \theta_B$. In this case, we have $\mu_2 = N_H$, $\mu_3 = N_V$, and $\mathbb{V}[v] = 0$. From Lemma 1, we obtain the mean

$$\begin{aligned} \mathbb{E}[\beta(R_E, \theta_E)] &= \frac{\mu_1}{\sqrt{M}} \sqrt{L_G(R_1)L_H(R_E)} \frac{(2M_s - M)(2N_s - N)}{M}, \end{aligned} \quad (60)$$

while the variance is

$$\begin{aligned} \mathbb{V}[\beta(R_E, \theta_E)] &= \frac{1}{M} L_G(R_1) L_H(R_E) \mathbb{V}[u] |\mathbb{E}[v]|^2 \\ &= L_G(R_1) L_H(R_E) 4 \frac{M_s(M-M_s)}{M^2(M-1)} \left(M - \frac{1}{M} \mu_1^2\right) (2N_s - N)^2. \end{aligned} \quad (61)$$

By substituting (60) and (61) into (34), we observe

$$\begin{aligned} \gamma_E^* &= \frac{P \frac{\mu_1^2}{M} L_G(R_1) L_H(R_E) \frac{(2M_s-M)^2 (2N_s-N)^2}{M^2}}{P L_G(R_1) L_H(R_E) 4 \frac{M_s(M-M_s)}{M^2(M-1)} \left(M - \frac{1}{M} \mu_1^2\right) (2N_s - N)^2 + \sigma_E^2} \\ &\leq \frac{P \frac{\mu_1^2}{M} L_G(R_1) L_H(R_E) \frac{(2M_s-M)^2 (2N_s-N)^2}{M^2}}{P L_G(R_1) L_H(R_E) 4 \frac{M_s(M-M_s)}{M^2(M-1)} \left(M - \frac{1}{M} \mu_1^2\right) (2N_s - N)^2} \\ &= \frac{\mu_1^2 (2M_s - M)^2 (M - 1)}{4M_s(M - M_s)M \left(M - \frac{1}{M} \mu_1^2\right)} \\ &< \frac{\max_{R_E}(\mu_1^2) (2M_s - M)^2 (M - 1)}{4M_s(M - M_s)(M^2 - \max_{R_E}(\mu_1^2))}. \end{aligned} \quad (62)$$

Here, if Eve is within the wiretap area, the maximum value of μ_1^2 occurs when $2\pi M \Delta F \frac{R_E - R_B}{c} = \pm 3\pi$. This point is exactly the midpoint between the first and second null of μ_1 . Thus, we have

$$\max_{(\theta_E, R_E) \in \mathcal{R}} \mu_1^2 = \left(\frac{\sin(\pm \frac{3\pi}{2})}{\sin(\pm \frac{3\pi}{2M} \pi)} \right)^2 = \frac{1}{\sin^2(\frac{3\pi}{2M})}. \quad (63)$$

Next, by substituting (63) in (62), we observe (43) in Lemma 3. Similarly, if $R_E = R_B$, we have

$$\begin{aligned} \gamma_E^* &< \frac{(2N_s - N)^2 (M - 1) \max_{\theta_E}(\mu_2^2 \mu_3^2)}{4N_s(N - N_s)(N^2 - \max_{\theta_E}(\mu_2^2 \mu_3^2))} \\ &= \frac{(2N_s - N)^2 (M - 1) \lambda^2}{4N_s(N - N_s)(N^2 - \lambda^2)}, \end{aligned} \quad (64)$$

where $\lambda = \max_{\theta_E} |\mu_2(\theta_E) \mu_3(\theta_E)|$, for $(\theta_E, R_E) \in \mathcal{R}$. However, an accurate closed-form for λ is challenging to observe. Thus, we approximate λ as $\lambda = \max(\lambda_1, \lambda_2)$, where λ_1 and λ_2 are obtained as $|\mu_2(\hat{\theta}_E)| |\mu_3(\hat{\theta}_E)|$ and $|\mu_2(\hat{\theta}_E)| |\mu_3(\hat{\theta}_E)|$, respectively. Here, $|\mu_2(\theta_E)|$ and $|\mu_3(\theta_E)|$ achieve their maxima at $\hat{\theta}_E$ and $\hat{\theta}_E$, respectively. Similar to (63), we obtain $\max(|\mu_2|) = \frac{1}{\sin(\frac{3\pi}{2N_H})}$,

which is observed when $N_H \pi (\cos \theta_B - \cos \theta_E) = \pm 3\pi$. As a result, we obtain $\theta_E = \arccos(\cos \theta_B \pm \frac{3}{N_H})$. Thereby, $\lambda_1 = \frac{1}{\sin(\frac{3\pi}{2N_H})} \frac{\sin(0.5N_V \pi (\sin \theta_E - \sin \theta_B))}{\sin(0.5\pi (\sin \theta_E - \sin \theta_B))} =$

$$\frac{\sin(0.5N_V \pi (\sqrt{1 - (\cos \theta_B \pm \frac{3}{N_H})^2} - \sin \theta_B))}{\sin(\frac{3\pi}{2N_H}) \sin(0.5\pi (\sqrt{1 - (\cos \theta_B \pm \frac{3}{N_H})^2} - \sin \theta_B))}, \text{ as we have}$$

$$\sin(\arccos(\cos \theta_B \pm \frac{3}{N_H})) = \sqrt{1 - (\cos \theta_B \pm \frac{3}{N_H})^2}.$$

Using the same approach, we obtain $\lambda_2 =$

$$\frac{\sin(0.5N_H \pi (\cos \theta_B - \sqrt{1 - (\sin \theta_B \pm \frac{3}{N_V})^2}))}{\sin(\frac{3\pi}{2N_V}) \sin(0.5\pi (\cos \theta_B - \sqrt{1 - (\sin \theta_B \pm \frac{3}{N_V})^2}))}.$$

D. Proof of Theorem 1

We define the objective of (46) as a function of the parameter M_s written as

$$\begin{aligned} f(M_s) &= \log_2(1 + \gamma_B^*) - \log_2\left(1 + \gamma_E^{\text{UB},1}\right) \\ &= \log_2\left(1 + \frac{P}{\sigma_B^2} L_G(R_1) L_H(R_B) \frac{(2M_s - M)^2}{M} (2N_s - N)^2\right) \\ &\quad - \log_2\left(1 + \frac{(2M_s - M)^2 (M - 1)}{4M^2 M_s (M - M_s) \sin^2(\frac{3\pi}{2M})}\right) \\ &= \log_2(1 + \eta_B (2M_s - M)^2) \\ &\quad - \log_2\left(1 + \eta_E \frac{(2M_s - M)^2}{4M_s (M - M_s)}\right), \end{aligned} \quad (65)$$

where $\eta_B = \frac{P}{\sigma_B^2} L_G(R_1) L_H(R_B) \frac{1}{M} (2N_s - N)^2$ and $\eta_E = \frac{(M-1)}{M^2 \sin^2(\frac{3\pi}{2M}) - 1}$ are two auxiliary parameters. Note that η_B and η_E are independent of M_s . The optimal M_s that maximizes $f(M_s)$ can be found by solving $\frac{\partial f(M_s)}{\partial M_s} = 0$, which is equivalent to

$$16\eta_B M_s^2 (M - M_s)^2 - \eta_B \eta_E (2M_s - M)^4 - M^2 \eta_E = 0. \quad (66)$$

In order to solve (66), we introduce a parameter $\tilde{M}_s = 2M_s - M$. Thereby, we have $M_s(M - M_s) = (\frac{M}{2} + \frac{\tilde{M}_s}{2})(\frac{M}{2} - \frac{\tilde{M}_s}{2})$. Thus, (66) can be written as

$$\eta_B (M^2 - \tilde{M}_s^2)^2 - \eta_B \eta_E \tilde{M}_s^4 - M^2 \eta_E = 0, \quad (67)$$

whose solution is given by $\tilde{M}_s^* = M \sqrt{\frac{1 - \frac{1}{M} \sqrt{\eta_B^{-1} \eta_E (\eta_E - 1) + M^2}}{1 - \eta_E}}$. As a result, the optimal value of M_s can be observed by $M_s^* = \frac{1}{2}(\tilde{M}_s^* + M)$. That completes the proof of (48). By following the same approach, we obtain the optimal value of N_s that maximizes the objective of (47) given by (49).

REFERENCES

- [1] D. P. Osorio, J. D. Sánchez, and H. Alves, "Physical-Layer Security for 5G and Beyond," *Wiley 5G Ref: The Essential 5G Reference Online*, pp. 1–19, 2019.
- [2] H. V. Poor and R. F. Schaefer, "Wireless physical layer security," *Proc. Natl. Acad. Sci. U.S.A.*, vol. 114, no. 1, pp. 19–26, 2017.
- [3] Y. Wu, A. Khisti, C. Xiao, G. Caire, K. K. Wong, and X. Gao, "A survey of physical layer security techniques for 5G wireless networks and challenges ahead," *IEEE J. Sel. Areas Commun.*, vol. 36, no. 4, pp. 679–695, 2018.
- [4] E. Jorswieck, S. Tomasin, and A. Sezgin, "Broadcasting Into the Uncertainty: Authentication and Confidentiality by Physical-Layer Processing," *Proc. IEEE*, vol. 103, no. 10, pp. 1702–1724, 2015.
- [5] K. Weinberger, S. Tewes, J. Müller, R. Dyrka, M. Mönnigmann, and A. Sezgin, "Flying Intelligent Surfaces: Joint Adjustment of Position and Configuration for UAV-Mounted RIS," in *Proc. IEEE 97th Veh. Technol. Conf. (VTC2023-Spring)*, 2023, pp. 1–5.
- [6] C. Li, M. van Delden, A. Sezgin, T. Musch, and Z. Han, "IRS-Assisted MISO System With Phase Noise: Channel Estimation and Power Scaling Laws," *IEEE Trans. Wirel. Commun.*, vol. 22, no. 6, pp. 3927–3941, 2023.
- [7] K. Zhi, C. Pan, H. Ren, and K. Wang, "Uplink Achievable Rate of Intelligent Reflecting Surface-Aided Millimeter-Wave Communications With Low-Resolution ADC and Phase Noise," *IEEE Wirel. Commun. Lett.*, vol. 10, no. 3, pp. 654–658, 2021.
- [8] K. Weinberger, R.-J. Reifert, A. Sezgin, and E. Basar, "RIS-enhanced Resilience in Cell-Free MIMO," in *Proc. 26th Int. ITG Workshop Smart Antennas (WSA) and 13th Conf. Syst., Commun., and Coding (SCC)*, 2023, pp. 1–6.

- [9] E. Čišija, A. M. Ahmed, A. Sezgin, and H. Wymeersch, "RIS-aided mmWave MIMO radar system for adaptive multi-target localization," in *Proc. IEEE Statist. Signal Process. Workshop (SSP)*, 2021, pp. 196–200.
- [10] H. Zhang, B. Di, K. Bian, Z. Han, H.V. Poor, and L. Song, "Toward ubiquitous sensing and localization with reconfigurable intelligent surfaces," *Proc. IEEE*, vol. 110, no. 9, pp. 1401–1422, 2022.
- [11] S. Tewes, M. Heinrichs, R. Kronberger, and A. Sezgin, "IRS-enabled breath tracking with colocated commodity WiFi transceivers," *IEEE Internet Things J.*, vol. 10, no. 8, pp. 6870–6886, 2022.
- [12] F. Lotfi, K. Weinberger, S. Roth, and A. Sezgin, "Under Whose Umbrella: The Collaborative Benefits of RS and RIS in Covert Communications," in *Proc. IEEE 24th Int. Workshop Signal Process. Advances in Wirel. Commun. (SPAWC)*, 2023, pp. 241–245.
- [13] C. Li and A. Sezgin, "IRS-Assistance with Outdated CSI: Element Subset Selection for Secrecy Performance Enhancement," in *Proc. IEEE Int. Conf. Commun. (ICC)*, 2023, pp. 2933–2938.
- [14] P. Staat, S. Mulzer, S. Roth, V. Moonsamy, M. Heinrichs, R. Kronberger, A. Sezgin, and C. Paar, "IRShield: A countermeasure against adversarial physical-layer wireless sensing," in *Proc. IEEE Symp Sec. Priv. (SP)*, 2022, pp. 1705–1721.
- [15] K. Feng, X. Li, Y. Han, S. Jin, and Y. Chen, "Physical Layer Security Enhancement Exploiting Intelligent Reflecting Surface," *IEEE Commun. Lett.*, vol. 25, no. 3, pp. 734–738, 2021.
- [16] J. Qiao and M. S. Alouini, "Secure transmission for intelligent reflecting surface-assisted mmWave and terahertz systems," *IEEE Wirel. Commun. Lett.*, vol. 9, no. 10, pp. 1743–1747, 2020.
- [17] B. Ning, Z. Chen, W. Chen, and L. Li, "Improving Security of THz Communication with Intelligent Reflecting Surface," in *Proc. IEEE Globecom Workshops (GC Wkshps)*, 2019, pp. 1–6.
- [18] S. Hong, C. Pan, H. Ren, K. Wang, and A. Nallanathan, "Artificial-noise-aided secure MIMO wireless communications via intelligent reflecting surface," *IEEE Trans. Commun.*, vol. 68, no. 12.
- [19] X. Guan, Q. Wu, and R. Zhang, "Intelligent reflecting surface assisted secrecy communication: Is artificial noise helpful or not?," *IEEE Wirel. Commun. Lett.*, vol. 9, no. 6, pp. 778–782, 2020.
- [20] G. C. Alexandropoulos, K. Katsanos, M. Wen, and D. B. Da Costa, "Safeguarding MIMO Communications with Reconfigurable Metasurfaces and Artificial Noise," in *Proc. IEEE Int. Conf. Commun. (ICC)*, 2021, pp. 1–6.
- [21] J. Lin, Q. Li, and J. Yang, "Frequency diverse array beamforming for physical-layer security with directionally-aligned legitimate user and eavesdropper," in *Proc. 25th Eur. Signal Process. Conf. (EUSIPCO)*, 2017, pp. 2166–2170.
- [22] J. Lin, Q. Li, J. Yang, H. Shao, and W.-Q. Wang, "Physical-Layer Security for Proximal Legitimate User and Eavesdropper: A Frequency Diverse Array Beamforming Approach," *IEEE Trans. Inf. Forensics Secur.*, vol. 13, no. 3, pp. 671–684, 2018.
- [23] Q. Cheng, S. Wang, V. Fusco, F. Wang, J. Zhu, and C. Gu, "Physical-layer security for frequency diverse array-based directional modulation in fluctuating two-ray fading channels," *IEEE Trans. Wirel. Commun.*, vol. 20, no. 7, pp. 4190–4204, 2021.
- [24] Y. Zhang, Y. Zhang, J. Wang, S. Xiao, and W. Tang, "Distance-Angle Beamforming for Covert Communications via Frequency Diverse Array: Towards Two-Dimensional Covertiness," *IEEE Trans. Wirel. Commun.*, pp. 1–1, 2023.
- [25] P. Antonik, M. C. Wicks, H. D. Griffiths, and C. J. Baker, "Frequency diverse array radars," in *Proc. IEEE Conf. on Radar*, 2006, pp. 3 pp.–.
- [26] J. Farooq, M. A. Temple, and M. A. Saville, "Application of frequency diverse arrays to synthetic aperture radar imaging," in *Proc. IEEE Int. Conf. Electromagn. Adv. Appl.* IEEE, 2007, pp. 447–449.
- [27] J. Xu, G. Liao, S. Zhu, L. Huang, and H. C. So, "Joint range and angle estimation using MIMO radar with frequency diverse array," *IEEE Trans. Signal Process.*, vol. 63, no. 13, pp. 3396–3410, 2015.
- [28] W.-Q. Wang, "Overview of frequency diverse array in radar and navigation applications," *IET Radar, Sonar Navig.*, vol. 10, no. 6, pp. 1001–1012, 2016.
- [29] W.-Q. Wang, H. C. So, and H. Shao, "Nonuniform Frequency Diverse Array for Range-Angle Imaging of Targets," *IEEE Sensors Journal*, vol. 14, no. 8, pp. 2469–2476, 2014.
- [30] J. Hu, S. Yan, F. Shu, J. Wang, J. Li, and Y. Zhang, "Artificial-Noise-Aided Secure Transmission With Directional Modulation Based on Random Frequency Diverse Arrays," *IEEE Access*, vol. 5, pp. 1658–1667, 2017.
- [31] B. Qiu, L. Wang, J. Xie, Z. Zhang, Y. Wang, and M. Tao, "Multi-Beam Index Modulation With Cooperative Legitimate Users Schemes Based on Frequency Diverse Array," *IEEE Trans. Veh. Technol.*, vol. 69, no. 10, pp. 11028–11041, 2020.
- [32] L. Li, Z. Chen, R. Chen, L. Yang, and S. Yan, "Covert wireless communication with random frequency diverse array," *IEEE Trans. Veh. Technol.*, vol. 73, no. 1, pp. 1473–1478, 2024.
- [33] K. Weinberger, A. A. Ahmad, A. Sezgin, and A. Zappone, "Synergistic Benefits in IRS- and RS-Enabled C-RAN With Energy-Efficient Clustering," *IEEE Trans. Wirel. Commun.*, vol. 21, no. 10, pp. 8459–8475, 2022.
- [34] N. Valliappan, A. Lozano, and R. W. Heath, "Antenna Subset Modulation for Secure Millimeter-Wave Wireless Communication," *IEEE Trans. Commun.*, vol. 61, no. 8, pp. 3231–3245, 2013.
- [35] N. N. Alotaibi and K. A. Hamdi, "Switched Phased-Array Transmission Architecture for Secure Millimeter-Wave Wireless Communication," *IEEE Trans. Commun.*, vol. 64, no. 3, pp. 1303–1312, 2016.
- [36] C. Rusu, N. González-Prelcic, and R. W. Heath, "An attack on antenna subset modulation for millimeter wave communication," in *Proc. IEEE Int. Conf. Acoust. Speech Signal Process. (ICASSP)*, 2015, pp. 2914–2918.
- [37] Y. Hong, X. Jing, and H. Gao, "Programmable Weight Phased-Array Transmission for Secure Millimeter-Wave Wireless Communications," *IEEE J. Sel. Top. Signal Process.*, vol. 12, no. 2, pp. 399–413, 2018.
- [38] M. E. Eltayeb, J. Choi, T. Y. Al-Naffouri, and R. W. Heath, "Enhancing Secrecy With Multiantenna Transmission in Millimeter Wave Vehicular Communication Systems," *IEEE Trans. Veh. Technol.*, vol. 66, no. 9, pp. 8139–8151, 2017.
- [39] B. You, I.-H. Lee, and H. Jung, "Optimal Subset Size Analysis of Randomized Analog Beamforming Using Uniform Planar Arrays in mmWave Networks," *IEEE Wireless Commun. Lett.*, vol. 10, no. 7, pp. 1414–1418, 2021.
- [40] Y. Hong, X. Jing, H. Gao, and Y. He, "Fixed region beamforming using frequency diverse subarray for secure mmWave wireless communications," *IEEE Trans. Inf. Forensics Secur.*, vol. 15, pp. 2706–2721, 2020.
- [41] S. Rangan, T. S. Rappaport, and E. Erkip, "Millimeter-Wave Cellular Wireless Networks: Potentials and Challenges," *Proc. IEEE*, vol. 102, no. 3, pp. 366–385, 2014.
- [42] B. Zheng and R. Zhang, "Intelligent Reflecting Surface-Enhanced OFDM: Channel Estimation and Reflection Optimization," *IEEE Wirel. Commun. Lett.*, vol. 9, no. 4, pp. 518–522, 2020.
- [43] C. Wu, X. Mu, Y. Liu, X. Gu, and X. Wang, "Resource Allocation in STAR-RIS-Aided Networks: OMA and NOMA," *IEEE Trans. Wirel. Commun.*, vol. 21, no. 9, pp. 7653–7667, 2022.
- [44] S. Lin, B. Zheng, G. C. Alexandropoulos, M. Wen, F. Chen, and S. Mumtaz, "Adaptive Transmission for Reconfigurable Intelligent Surface-Assisted OFDM Wireless Communications," *IEEE J. Sel. Areas Commun.*, vol. 38, no. 11, pp. 2653–2665, 2020.
- [45] S. Shen, B. Clerckx, and R. Murch, "Modeling and Architecture Design of Reconfigurable Intelligent Surfaces Using Scattering Parameter Network Analysis," *IEEE Trans. on Wirel. Commun.*, vol. 21, no. 2, pp. 1229–1243, 2022.
- [46] A. D. Wyner, "The wire-tap channel," *Bell Sys. Tech. J.*, vol. 54, no. 8, pp. 1355–1387, 1975.
- [47] D. Tse and P. Viswanath, *Fundamentals of wireless communication*, Cambridge University Press, 2005.
- [48] Q. Wu and R. Zhang, "Intelligent reflecting surface enhanced wireless network via joint active and passive beamforming," *IEEE Trans. Wirel. Commun.*, vol. 18, no. 11, pp. 5394–5409, 2019.
- [49] F. Naeem, M. Ali, G. Kaddoum, C. Huang, and C. Yuen, "Security and Privacy for Reconfigurable Intelligent Surface in 6G: A Review of Prospective Applications and Challenges," *IEEE Open J. Commun. Soc.*, 2023.
- [50] J. D. Kraus and R. J. Marhefka, "Antennas for all applications," *Antennas for all applications*, 2002.
- [51] N. S. Perović, L. N. Tran, M. Di Renzo, and M. F. Flanagan, "Achievable Rate Optimization for MIMO Systems With Reconfigurable Intelligent Surfaces," *IEEE Trans. Wirel. Commun.*, vol. 20, no. 6, pp. 3865–3882, 2021.
- [52] X. Ma, Z. Chen, W. Chen, Z. Li, Y. Chi, C. Han, and S. Li, "Joint Channel Estimation and Data Rate Maximization for Intelligent Reflecting Surface Assisted Terahertz MIMO Communication Systems," *IEEE Access*, vol. 8, pp. 99565–99581, 2020.
- [53] H. Du, J. Zhang, K. Guan, D. Niyato, H. Jiao, Z. Wang, and T. Kürner, "Performance and optimization of reconfigurable intelligent surface aided thz communications," *IEEE Trans. Commun.*, vol. 70, no. 5, pp. 3575–3593, 2022.
- [54] D. G. Horvitz and D. J. Thompson, "A generalization of sampling without replacement from a finite universe," *J. Am. Statist. Assoc.*, vol. 47, no. 260, pp. 663–685, 1952.